Boron Monolayer Doping; Role of Oxide Capping Layer, Molecular Fragmentation and Doping Uniformity at the Nanoscale

Avra Tzaguy[1], Dr. Prajith Karadan[1], Dr. Krushnamurty Killi[1], Dr. Ori Hazut[1], Dr. Iddo Amit[2], Prof. Yossi Rosenwaks[2] and Prof. Roie Yerushalmi[1,]*

[1] Institute of Chemistry and the Center for Nanoscience and Nanotechnology, The Hebrew University of Jerusalem, Edmond J. Safra Campus, Givat Ram Jerusalem, 91904 Israel

[2] Department of Physical Electronics – School of Electrical Engineering, Tel Aviv University, Ramat Aviv 69978, Israel

* E-mail: roie.yerushalmi@mail.huji.ac.il

Keywords: Doping, Nanowires, Monolayer, Boron, KPFM

Abstract

Doping methodologies using monolayers offer controlled, *ex-situ* doping of NWs and 3D device architectures using molecular monolayers as dopant sources with uniform, self-limiting characteristics. Comparing doping levels and uniformity for boron containing monolayers using different methodologies demonstrate the effects of oxide capping on doping performances following rapid thermal anneal (RTA). Strikingly, for non-covalent monolayers of phenyl-boronic acid (PBA), highest doping levels are obtained with minimal thermal budget without applying the oxide capping layer. These results are accounted for by considering monolayer damage and entrapment of molecular fragments in the oxide capping layer because thermal damage to the PBA monolayer which result in transformation of the monolayer source to a thin solid source layer. The impact of the oxide capping procedure is demonstrated by a series of experiments. Details of monolayer fragmentation processes and its impact on doping uniformity at the nanoscale are addressed for two types of surface chemistries by applying Kelvin probe force microscopy (KPFM). Our results point at the importance of molecular decomposition processes for monolayer-based doping methodologies, both during pre-anneal capping step and during rapid thermal processing step. These are important guidelines to be considered for future developments of appropriate surface chemistry used in monolayer doping applications.

1. Introduction

Semiconducting nanowires (SC-NWs) are central building blocks for the realization of electronic devices in emerging applications. To date, the use of SC-NWs have been demonstrated for numerous applications such as optoelectronic devices, reconfigurable electronics, sensors, photovoltaics and more.[1–9] Most NW-based electronic devices requires precise distribution of dopants since device functionality relies on the formation of well-defined doping profiles. Local stochastic fluctuations in doping densities have been shown to produce a large variance in device characteristics and performance.[5,10]

In-situ doping of silicon NWs in general, and of boron doping (p-type) in particular, where dopant atoms are introduced during the growth process is widely established.[5] However, the fabrication of uniformly-doped p-type boron doped NWs and formation of sharp p-i-n junctions across NWs still poses challenging tasks using conventional *in-situ* doping methods. These difficulties arise since the incorporation of impurity atoms such as boron precursors at the CVD growth chamber while depositing the SC affects the quality and crystallinity of the NWs. Several studies addressed specific aspects of the complications involved in the *in-situ* boron doping of NWs, for example, Ma *et al.* showed the formation of several defect types, including nanoparticle formation at the NW surface as well as polycrystalline rectangular nanoscale domains for *in-situ* boron-doped SiNWs. These phenomena are explained by surface segregation of boron and surface reconstruction of the SiNW crystalline structure accompanying the *in-situ* process in the presence of boron impurities.[11] In addition, Pan *et al.* reported the formation of a core-shell structure with a thick amorphous Si shell surrounding the crystalline Si core for SiNWs deposited under high partial pressures of diborane (B_2H_6) and trimethylboron ($B(CH_3)_3$), which are commonly used for *in-situ* doping of SiNWs.[12] The same group reported also the accumulation of Au atoms at the outer surface of the NWs during the CVD synthesis, which was attributed to the increased rate of Si deposition at the NW surface.[12]

Therefore, separation of the incorporation of impurity atoms required for doping from the SC synthesis step is crucial for avoiding some of the complications involved in the commonly used *in-situ* doping process. Conventional *ex-situ* doping techniques such as ion implantation are of limited effectiveness for addressing the difficulties that arise for doping nanostructures because of the lattice damage, amorphization, and stochastic fluctuations that are typically involved when applying these methods to nanostructures.[10,13–15] Monolayer doping (MLD)[14] and monolayer contact doping (MLCD)[16,17] techniques offers a substantial advancement toward the controlled, *ex-situ* doping of NWs. These methods use molecular monolayers as uniform, self-limiting diffusion source for dopants. Furthermore, monolayer doping methods are useful in lowering the thermal budget of dopant diffusion and activation, which is most critical for NW applications and 3D MOSFET devices.[18,19] In MLCD, the dopants are introduced into the SC by forming monolayer with molecular components that contain dopant atoms in their structure which are released when the substrate is heated in a rapid thermal anneal (RTA) step. The monolayer is formed on a wafer, termed the "donor wafer". The donor wafer is pressed against a second wafer (termed "target wafer"), intended for doping, and possibly on which NWs are deposited prior to the doping process. Next, the two wafers are annealed using RTA furnace, and finally separated. Using the MLCD technique, we have demonstrated that phosphorus doping produces a highly-uniform longitudinal distribution of dopants along the NW.[16]

Monolayer doping is used in an increasing number of applications that require the controlled doping of nanostructures and for achieving ultra-shallow surface doping of semiconductors.[20–25] Advances in monolayer doping provide significant progress in obtaining improved properties, including higher doping densities and various aspects of the monolayer doping method.[18,26] Monolayer doping involves the thermal fragmentation of the monolayer followed by dopant activation and diffusion. To date, most reports focus on studying the influence of surface chemistry used, molecular footprint, and details of capping layer used on

the resulting doping levels.[18,27–32] The application of phenyl boronic acid (PBA) monolayers in doping was previously studied, in part, for the formation of sharp p-i-n junctions in SiNWs,[17] for studying dopant diffusion and activation in SiNWs, [33] and for dopant patterning. [34] Herein, a systematic study to understand the impact of oxide cap deposition on the B-doping by PBA monolayer is presented. We demonstrate that oxide cap deposition may damage the PBA monolayer, which is attributed to the elevated temperatures required for the deposition process prior to the thermal anneal and activation step. Therefore, in some cases higher doping levels are attainable without applying oxide capping layer.

2. Results and Discussion

2.1. Comparison of monolayer doping methods using PBA monolayers

PBA monolayers were previously studied as dopant source for monolayer doping (MLD),[14] monolayer contact doping (MLCD),[16] and remote-monolayer doping (R-MLD)[34] techniques. Thorough discussion of monolayer doping methodologies and state-of-the art in the field can be found elsewhere.[35] Briefly, the key difference between MLD and the other two techniques discussed here is the deposition of SiO_2 capping layer on the dopant containing monolayer for MLD, while no capping is applied for MLCD and R-MLD. Instead, a target substrate is placed on top of the donor substrate in direct contact for MLCD. R-MLD is similar to MLCD except for a separator mask that is placed between the donor and acceptor substrates, see **Figure 1** for details. Comparing sheet resistance values obtained for PBA by applying the three methods point at processes taking place both during the rapid thermal anneal and during the oxide layer capping steps.

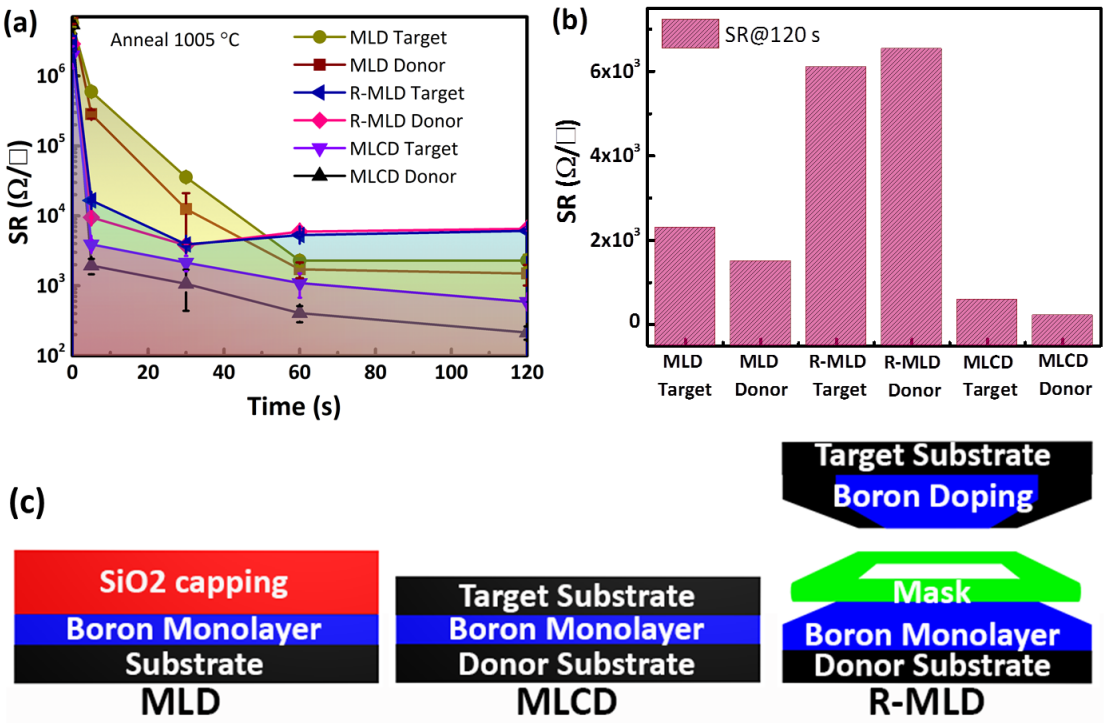

Figure 1. Comparison of monolayer doping methods studied using PBA monolayers. (a) Sheet resistance as a function of anneal time for the three methods, (b) comparison of SR values across methods for long anneal time (120 s), (c) schematics of substrate details for the doping methods applied and terminology used for 'donor' and 'target'.

Highest doping levels (lowest SR values) were obtained for MLCD for which no oxide capping layer is applied as expressed by comparison of the SR values for long anneal time (120 s), Figure 1b. Furthermore, not only the lowest SR is obtained for MLCD at long anneal time, but also the fastest decrease in SR is obtained for short anneal times. Comparing SR values across the techniques for any given anneal time presented in Figure 1a show consistent trend following the order (ordered from lowest SR to high): MLCD Donor < MLCD Target < R-MLD Donor ≈ R-MLD Target < MLD Donor < MLD Target. This is further visualized by the marked areas below the curves in Figure 1a. This result is counter-intuitive as the trend observed is opposite to the expected behavior considering the role of oxide capping layer in the prevention of loss of volatile fragments and dopants to the anneal chamber. For 60 and 120s the trend is changed between MLD and R-MLD with the latter more resistive, and MLCD

remaining the lowest resistive SR values. This is explained by considering mass transfer mechanisms for the R-MLD method which is restricted to vapor phase, owing to the physical separation between the donor and target substrates, unlike the MLCD and MLD which involve solid-solid diffusion. Therefore, for long anneal times, for R-MLD no dopants are activated since all available dopants in the vapor phase are consumed or lost during the initial ramp, unlike for the other two methods.[34]

2.2. Effect of oxide capping layer on PBA monolayer doping

The effect of depositing oxide capping layer on top of PBA monolayers was studied by the application of several oxide deposition schemes. For SiO_2 deposited by evaporation, it was found that SR values increased as the oxide layer thickness increased (**Figure 2**a). This result is consistent with the comparison of SR values obtained for MLD and MLCD, further demonstrating that the oxide cap layer functions not only as a barrier to prevent dopant atoms from diffusing away to the anneal chamber during the RTA step, but also entraps the boron atoms in the deposited oxide layer because of the thermal damage to the monolayer during the oxide deposition step. This is consistent with the non-covalent nature of the PBA monolayer assembly which will be discussed in section 2.4. A second SiO_2 evaporation scheme was tested termed as 'Two step capping', applying initial deposition of a thin oxide layer, allowing it to cool to room temperature and solidify, then depositing a second SiO_2 layer such that the total thickness of both deposited layers was kept constant at 25 nm. The two-step evaporation resulted in similar trend for SR values as for the one-step evaporation with increasing SR for a given anneal time and temperature with the total oxide cap thickness (Figure 2b). Notably, both the fastest initial decrease in SR and lowest values for long anneal times were obtained for un-capped samples (termed '0 nm' in Figures 2(a-d)), similar to the results obtained by comparison of MLCD to MLD. Our data demonstrate that for PBA, which is a non-covalent monolayer assembly, it is preferable to avoid oxide capping for attaining the highest doping levels and lowest thermal budget for a given doping level. This result can be rationalized by considering

the thermal damage to the PBA monolayer inflicted by the thermal evaporation of the oxide and the labile diffusion of fragmentation products in the hot oxide during the evaporation process. Therefore, in effect, applying oxide evaporation for capping a non-covalent monolayer yields a thin solid source rather than a monolayer source for monolayer doping methodologies. This result should be further studied to generalize it to other types of monolayers and surface chemistries. In order to avoid the thermal effects associated with the oxide evaporation method we tested atomic layer deposition (ALD) of SiO_2 where substrate reaction temperature is limited to 250 ^{o}C (Figure 2e). The SR data show that for ALD, similar to oxide evaporation, SR values were higher (lower doping levels) compared to the non-capped samples but similar to the evaporated oxide (see Figure 2e, anneal times of 60 and 120 s). Furthermore, the initial drop in SR values was, again, highest for the non-capped MLCD-PBA compared to both evaporated and ALD-deposited SiO_2 capping layers. The lower doping levels obtained for the ALD SiO_2 cap may be attributed to both the fragmentation of the PBA monolayer as a result of ozone dosing used as an oxidizing agent in the SiO_2 ALD process, and to effective entrapment of the PBA monolayer and fragments in the high-quality pin-hole free SiO_2 layer, which is typical for ALD.

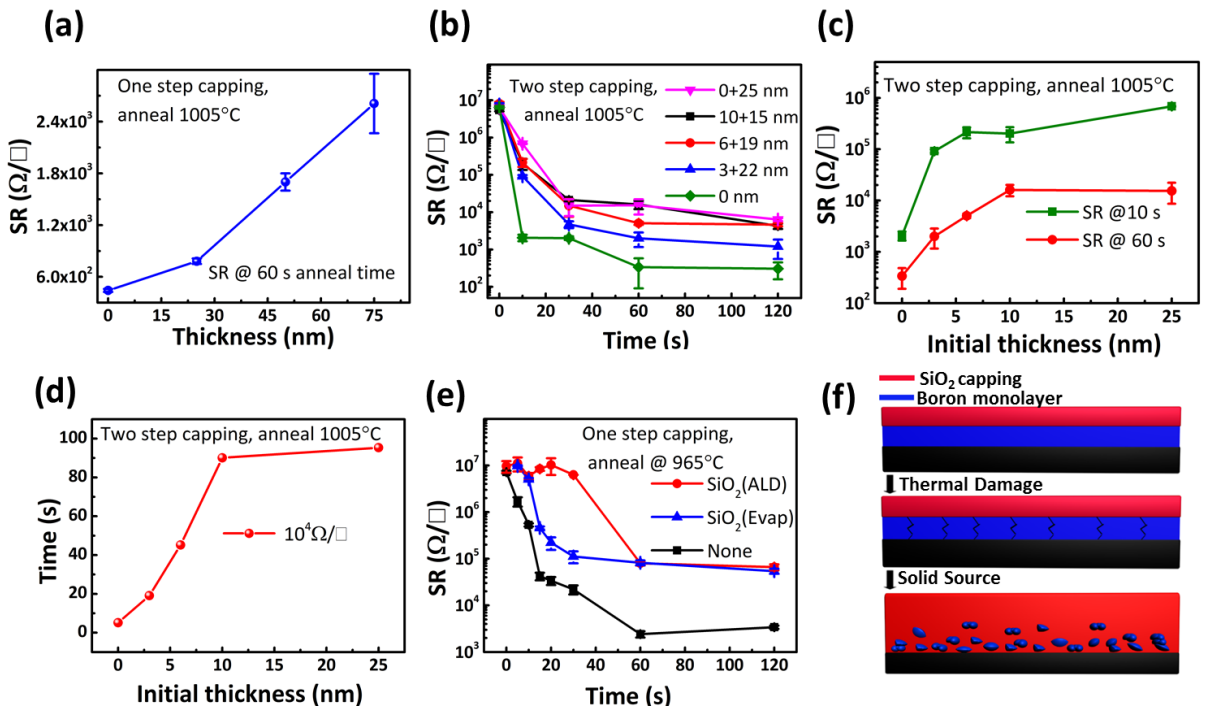

Figure 2. Sheet resistance obtained for doping with PBA monolayers using various oxide capping schemes. (a) SR reached after 60 s anneal for increasing oxide cap thickness, (b) SR vs. anneal time for two-step deposited oxide cap with constant total thickness of 25 nm, (c) SR vs. initial oxide cap thickness for constant anneal times of 10 and 60 s, (d) Time required to reach a threshold SR of 10^5 Ω/□ vs. initial oxide cap thickness, (e) SR vs. time for samples annealed at 965ºC with SiO_2 deposited by ALD, SiO_2 deposited by evaporation, and no capping layer obtained, (f) Proposed monolayer damage and encapsulation mechanism in the oxide capping layer.

2.3. Doping uniformity at the microscopic scale

Microscopic dopant distributions were studied using Kelvin probe force microscopy (KPFM) for *ex-situ* doping of silicon NW devices. Doping uniformity was studied by applying MLCD with PBA which form non-covalent monolayers, *vide infra* further details on PBA monolayer formation, and for chlorodicyclohexylborane (CDB) covalent monolayer for which the surface chemistry was previously studied in detail.[36]

The NW channel topography measured by AFM showed a smooth and clean surface, indicating that the doping process did not induce observable damage at the doped NW surface

(**Figure 3**a). For NW devices with a near-Ohmic behavior, where the majority of the potential drop occurs over the entire length of the resistor, the doping level can be derived using:

$$N_A^-(x) = \frac{J}{q\mu_p(N_A^-)\frac{d\Phi_s(x)}{dx}} \quad (1)$$

Where N_A^- is the active (ionized) acceptor density, and $\mu_p(N_A^-)$ is the hole mobility, corrected to the acceptor density, and $\frac{d\Phi_S(x)}{dx}$ is the gradient of the workfunction of the nanowire in the axial direction. In a homogeneous material, this is the equivalent of the electric field that drives the drift current. For PBA-MLCD doped NWs the contact potential difference (CPD) data (Figure 3b) showed local work function variations along the NW axis on the scale of ~10 mV, indicating that the doping level fluctuates along the axis were smaller in one order of magnitude compared to the average doping level. The average doping for the PBA-MLCD doped NWs is 7.5×10^{18} cm^{-3}, with the spatially resolved analysis showing that the doping levels were overall uniform with slight local variations along the NW axis at different positions. CPD line scans were measured with the left hand side electrode biased (Figure 3c) and the right hand side electrode biased (Figure 3d) to account for asymmetry in the device characteristics. While both graphs show a similar potential drop across the central portion of the NW, it is clear that there is a larger potential drop over the left Au electrode – NW interface than over the opposite interface. It is important to note that the analysis described in Equation (1) is valid only when describing a purely resistive behavior, i.e. away from the depletion region induced by the electrode-NW contacts. Notably, although the left interface is essentially a Schottky junction, producing a depletion region near the electrode as indicated by the band bending towards the metal, this junction resistance is negligible with regards to the resistance of the whole device and the majority of the potential drop occurs over the entire NW length.

For CDB-MLCD doped NWs the CPD profiles were consistent with those of an Ohmic resistor showing a linear potential drop over the central part of the wire, with an average doping

level of $1.5x10^{19}$ cm^{-3} for the CDB-MLCD doped NW, slightly higher than the doping levels obtained for the PBA-MLCD doped NWs. A comparison between the spatially resolved doping levels of the PBA- and CDB-MLCD doping applied to the nanowires is presented in Figure 3f. While the average doping levels obtained for the CDB-MLCD doped NWs were higher compared to PBA-MLCD, it also showed higher local variations in the hole density along the NW (Figures 3e,f) which could be the result of localized variations in doping density and/or a result of high local concentrations of charge traps. These local variations in the charge carrier densities are pointed by the red arrows (Figure 3e). Such abrupt local variations in charge densities affect the overall NW device resistivity and transport properties. Despite the high average doping level of CDB-MLCD doped NW, the large variations in the local hole density of these NW devices varying by a factor of 2 over less than 3 µm, lead to a higher overall resistivity of the CDB- compared to the PBA-MLCD doped NWs.

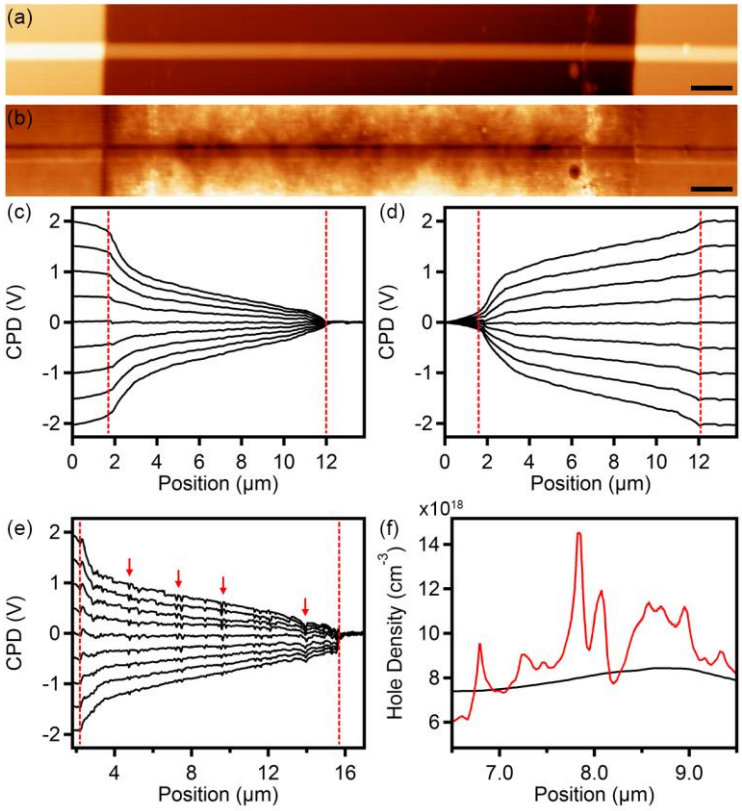

Figure 3. Scanning probe analysis of MLCD-doped NW devices. (a) 2D topography image, (b) CPD image of a typical PBA-MLCD doped NW device measured simultaneously with the

topography in a dual-frequency mode measurement (scale bar 1 μm). (c,d) CPD profiles obtained along the center of the PBA-MLCD doped NWs between the two electrodes, shown with the left hand side (c) and right hand side (d) electrode biased top to bottom 2V to -2V. The dashed red lines represent the location of the Au electrodes (e) CPD profiles obtained along the center of the CDB-MLCD doped NWs between both electrodes at 2V to -2V drain biases. Red arrows indicate local fluctuations of the CPD values along the NW and the red dashed line indicate the location of the Au electrodes (f) Comparison of the spatially resolved doping distribution for the PBA-MLCD doped NW (black curve) and CDB-MLCD doped NW (red curve).

2.4. Phenyl-boronic acid monolayer formation

To better understand the relationship between the surface chemistry used for the boron containing monolayer source and the resulting doping uniformity when applying the MLCD doping procedure, we further studied the solution and surface chemistry of SiO_2 NPs reacted with PBA, and with the trimer condensation product of PBA, boroxine anhydride, triphenylboroxine (TPB). The FTIR spectra of neat PBA, PBA reacted in mesitylene for 5 min, and of neat TPB are presented in **Figure 4**a. PBA showed the expected broad IR absorptions assigned to ν(O─H) and δ(B─O─H) modes at 3275 cm^{-1} and 1008 cm^{-1} , respectively.[37] In contrast, the broad O-H bands were completely absent for PBA reacted in mesitylene for 5 min and longer reaction times, and for TPB. Furthermore, the spectra obtained for TPB and PBA reacted in mesitylene were identical; both showing peaks assigned to the boroxole ring, δBO_2, out of plane deformation at 688 cm^{-1}.[37] These results show that PBA rapidly condense in mesitylene to form TPB, the trimer boroxine anhydride. Therefore, we suggest that PBA is rapidly reacting in solution resulting in the TPB within minutes, and that the monolayer is formed *via* TPB adsorption at the polar SiO_2 interface driven by hydrogen bonding and stacking interactions (Figure 4b). The ellipsometry results for both PBA and TPB reacted in mesitylene with silicon wafers with a thermal oxide layer showed self-limiting monolayer formation with typical reaction time of ~2 h required to reach maximal coverage (Figure 4c). Both the final thickness (~ 6Å) and reaction completion time (~2 h) were the same within experimental error for the two precursors, PBA and TPB, further supporting our conclusion that PBA initially form the TPB trimer within a few minutes, which adsorb at the polar oxide surface, with a slower rate, explaining the equal results obtained when using either PBA or TPB as precursors.

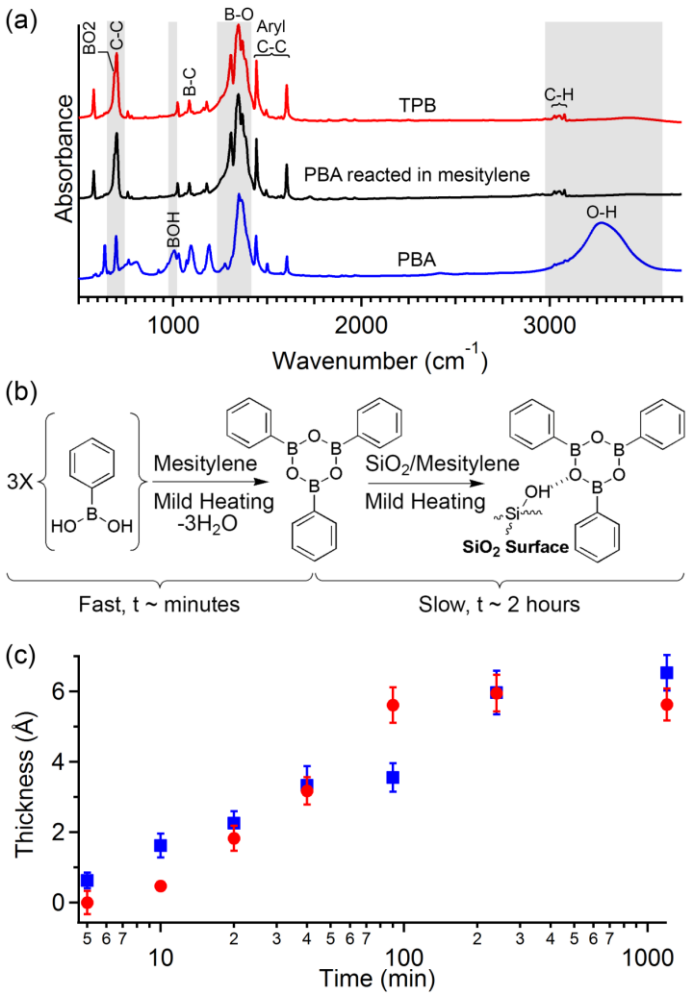

Figure 4. Self-limiting surface reactions of PBA and TPB with SiO_2 surfaces. (a) FTIR spectra for TPB, PBA reacted in mesitylene, and un-reacted PBA. PBA reacted in mesitylene showed identical spectra to TPB within 5 minutes indicating the rapid and full condensation of PBA to TPB. (b) PBA condenses in mesitylene within minutes to form the trimer TPB, which adsorb at the polar SiO_2 surface via H-bond interactions (shown) and possible stacking interactions between TPB molecules (not shown). (c) Thickness vs. reaction time for silicon wafers with thermal oxide reacted with the respective precursors in mesitylene for the specified time, PBA (●) and TPB (■) obtained by spectroscopic ellipsometry.

2.5. Phenyl-boronic acid monolayer fragmentation

Monolayer contact doping process involves fragmentation of the monolayer source during the rapid thermal anneal step where molecular components undergo thermal decomposition and further reactions with the interface, typically a thin SiO_2 layer, and diffusion into the silicon

lattice at the higher temperatures. The thermal decomposition and fragmentation of PBA non-covalent and CFM covalent monolayers were studied using FTIR and TGA-MS by reacting SiO_2 nanoparticles (NPs) with the respective boron precursors. The thermal fragmentation of the monolayers was studied by *in-situ* mass spectrometry to detect the volatile fragments evolved while ramping the temperature and simultaneously quantifying mass loss of the reacted NPs. PBA reacted SiO_2 NPs showed the expected weight change at ~100 °C indicative of loss of adsorbed water molecules. Further mass loss as a result of the decomposition of the monolayer components was observed by the weight changes commencing at ~200 °C, and completely decomposed up to 450 °C indicated by the gray regions in **Figures 5**a,b.

For PBA, the main mass detected corresponds to benzene ring fragment (m/z 78) with the expected additional signals for m/z of 50, 51, and 52, corresponding to the ring fragments C_4H_x (x=2-4),[38] and possibly, boron contacting fragments C_3H_xB (x=3-5) with the same masses (Figure 5a). The TGA-MS signals evolved simultaneously with temperature for the different m/z values detected with maximal signal intensity occurring concurrently for all peaks around 370 °C. Namely, the PBA fragmentation process takes place simultaneously for all detectable m/z values. In contrast, covalently grafted CDB monolayers showed thermal fragmentation with multiple steps with volatile fragments containing boron atoms detected at 300 °C, occurring during the temperature ramping between the carbon fragments peaks at 260, 280, and 410 °C. The peaks at 280 °C and 410 °C for m/z of 54, and 67, and a third maximum for m/z 82 at 260 °C corresponding to cyclohexene and related fragments, C_4H_6 and C_5H_7.[38] In addition, fragment with m/z of 78 was detected corresponding to C_5H_7B with intensity maximum obtained at 300 °C. The TGA-MS data show that the CDB monolayers undergo complex fragmentation processes during the thermal ramping with multiple steps occurring at different temperatures, whereas the PBA degradation evolved around a single temperature.

We suggest that the markedly different degradation processes for CDB compared to PBA revealed by TGA-MS analysis may account for the differences in doping uniformities

demonstrated by KPFM when the two types of monolayer were used using the same method, MLCD. The large fluctuations found for nanowires doped by CDB-MLCD revealed with the KPFM measurements may arise because of cluster formation at the Si/SiO_2 interface, possibly SiC, which may affect the local dopant distribution, diffusion, and activation. Furthermore, we previously demonstrated that the native oxide layer capture carbon impurities, thus functioning as a diffusion barrier for impurities owing to the limited diffusivity of the carbon impurities at the Si/SiO_2 interface, provided that the impurity dose is limited.[39] Overall, the combined data suggests that PBA assembles as TPB at the interface and the phenyl rings are cleaved around 370 °C leaving the boroxole framework consisting of only boron and oxygen atoms at the Si/SiO_2 interface. This results in the minimization of carbon cluster formation in the anneal process, by separating the monolayer fragmentation, cleavage of carbon-containing portions, and diffusion of the boron fragments through the native oxide layer when the ramping profile reaches the higher temperatures required for diffusion and activation, above 800 ºC. Thus the different decomposition processes and fragmentation details of the two types of molecular precursors used here affect the obtained doping uniformity by MLCD, which may be an important guideline to consider for future developments of appropriate surface chemistry for such applications.

FTIR spectroscopy was used for studying the evolution of surface species with monolayer anneal temperature for SiO_2 NPs reacted with TPB and PBA (Figure 5c). The FTIR spectra of as-prepared SiO_2 NPs reacted with TPB and PBA were identical for as-prepared monolayers (Figure 5c, trace shown for 40 °C), in agreement with the suggested pre-assembly condensation of PBA to the TPB trimer in solution, followed by monolayer formation at the SiO_2 NP surface.

The absorption peaks at ~ 3100 cm^{-1} correspond to aromatic ν(C─H), the broad bands around 1400 cm^{-1} correspond to ν(B─O), and the sharp peaks at 1441 and 1603 cm^{-1} confirm the presence of aryl group bonded to boron. Significant changes in the FTIR spectra were

observed for anneal temperatures exceeding 300 °C as expected from decomposition of the organic framework and additional processes that occur at the surface with the evolving fragments as demonstrated by the TGA-MS results. For anneal temperatures above 300 °C, all IR bands associated with ν(C─H), as well as the bands associated with the aryl functionality, were absent owing to the decomposition of the organic components (Figure 5c). Furthermore, the two peaks at 1342 and 1363 cm^{-1} observed at low temperatures (≤ 300 °C) evolved to a broad band at 1396 cm^{-1} indicative of B─O species.[40] The observed spectral changes in the region of 3200-4000 cm^{-1} are associated with alterations in the -OH hydrogen-bonding environment.[40,41]

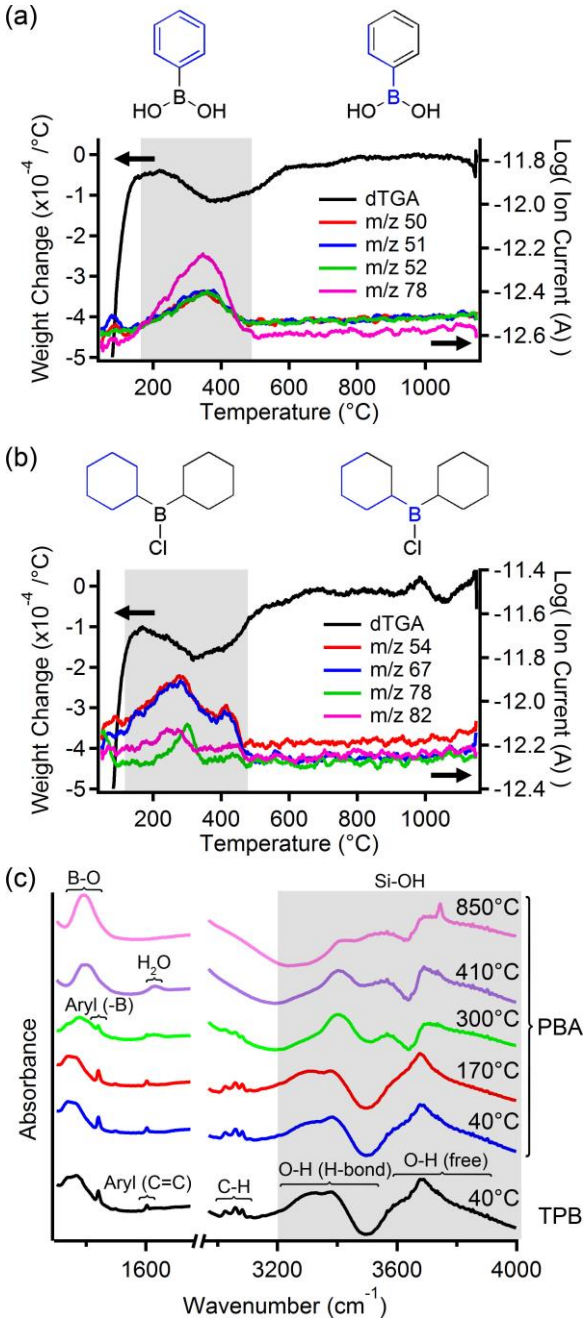

Figure 5. Thermogravimetric analysis coupled with mass spectrometry (TGA-MS) analysis for SiO_2 nanoparticles reacted with (a) PBA, and, (b) CDB (dTGA data shown in black). (c) FTIR spectra of SiO_2 NPs reacted with PBA and TPB, annealed at the specified temperatures under Argon. All FTIR data was collected at room temperature under vacuum.

3. Conclusions

In summary, *ex-situ* boron doping of silicon substrates, including planar and NW configurations were studied using MLD, MLCD, and R-MLD. The doping process was studied for both silicon wafers and NWs, characterized by macroscopic and local probe techniques, respectively. For PBA monolayers, it is shown that oxide deposited after monolayer formation functions not only as a capping layer, intended for enhancing doping levels, but it also entraps monolayer fragments, including boron atoms in the deposited oxide layer because of the thermal damage during the oxide deposition step. Therefore, *in effect*, depositing an oxide layer on the non-covalent PBA monolayer yields a thin solid source rather than a monolayer source for monolayer doping methodologies. This result should be further studied for other types of monolayers for better tuning of surface chemistries and process protocols applied in monolayer doping methodologies.

Microscopic mapping of doping surface distribution using KPFM showed that PBA-MLCD resulted in uniform dopant distributions while the CDB-MLCD doped NWs showed higher fluctuations in local dopant concentrations. The different monolayer sources were further considered by studying the decomposition of PBA and CDB by TGA-MS and FTIR. Our results show that both types of surface chemistries, both covalent and non-covalent assembly, provide high doping levels using the MLCD method, with similar SR values obtained by macroscopic measurements. However, the microscopic KPFM measurements revealed that the microscopic dopant distributions were highly dependent on the type of surface chemistry used and the details of the degradation process of the molecular precursors used for the monolayer source. The non-covalent approach using PBA yielded high-quality, uniform doping whereas the covalent surface chemistry approach using CDB resulted in large dopant fluctuations at the microscopic scale.

CDB monolayers undergo complex fragmentation processes during the thermal ramping with multiple steps occurring in several temperatures whereas PBA degradation evolved around a

single temperature region. For PBA we find that phenyl rings are cleaved at moderate temperatures, leaving the B-O boroxole frame at the Si/SiO_2 interface, therefore minimizing cluster formation by the time the anneal step reaches sufficient temperatures for boron diffusion through the native oxide layer. For CDB, in contrast, the mixed fragments containing both carbon and boron are detected, leading to the possible formation of silicon-carbide clusters that affect doping uniformity found by nanometer-resolution KPFM analysis.

Our results provide insights regarding the importance of designing not only the structural features of the precursor molecules and monolayer assembly by taking into account parameters such as molecular footprint and the stability of surface-molecule bonds, but also considering molecular fragmentation processes. These considerations are important for managing the retention of molecular fragments in the oxide layer and for minimizing fluctuations in the doping levels at the semiconductor surface. Therefore, consideration of the detailed molecular fragmentation processes may be an important guideline for future developments of appropriate surface chemistries for monolayer doping methodologies.

4. Experimental Section

Monolayer formation on Si wafers was performed for phenylboronic Acid (PBA, Sigma-Aldrich), triphenylboroxine (TPB, TCI) and chlorodicyclohexylborane (CDB, Sigma-Aldrich). Prior to monolayer formation, Si wafers were diced and cleaned in piranha solution (3:1 H_2SO_4 : 30% H_2O_2) for 15 min followed by basic piranha cleaning (5:1:1 H_2O : 27% NH_4OH : 30% H_2O_2) for 8 min in a sonication bath at 60 °C.

Caution: Piranha solutions are extremely strong and dangerous oxidizing agents and should be used with extreme caution. May explode in contact with organic solvents.

The cleaned substrates were immersed in mesitylene precursor solution. Freshly prepared mesitylene solutions of the respective precursors were used for reacting Si wafers (34.8 mM PBA, 11.6 mM TPB, and 77 mM CDB). The reaction was carried out in a sealed vial at 100 °C

for 2 hrs followed by rinsing in mesitylene (x3), dichloromethane (x3), and drying under N_2 flow. Further details including SiNW synthesis and annealing procedures as previously reported.[16,42]

Monolayer formation on SiO_2 nanoparticles was performed by reacting 100 mg of 15 nm nanoparticles in 10 mL of mesitylene precursor solution for 2 h at 100 °C. The supernatant solution was removed by centrifugation and washing with fresh mesitylene (x3) and followed by hexane washing (x3) followed by drying at 115 °C for 1 h.

FTIR analyses were performed using KBr pellets each containing 200 mg (Sigma-Aldrich) and 1 mg of bulk precursor compound or 2 mg of reacted SiO_2 nanoparticles using a Bruker vertex 70v spectrometer for FTIR measurements under vacuum.

Ellipsometric measurements were carried out using a J.A. Woolam Co. variable-angle VB-400 spectroscopic ellipsometry system (VASE). Measurements were performed using Si(100) substrates with 50 nm thermal oxide layer that were measured prior to- and immediately after monolayer formation.

TGA-MS analyses were performed using Netzsch Jupiter STA TG-DSC 449 F3 used for thermogravimetric analysis coupled with Netzch Aeolos QMS 403 D quadruple mass detector. Approximately 15 mg of the reacted SiO_2 nanoparticles were placed in an alumina crucible heated from 50 °C to 1150 °C (heating rate of 1.5 °C min^{-1}) and mass scan range of 1 to 300 a.m.u.

Rapid thermal anneal (RTA) was performed using AnnealSys AS-Micro system. The process chamber was purged in argon and evacuated to 0.05 mbar prior to the anneal process. Anneal was carried out by rapid heating to a desired temperature and further annealing for certain time as noted above.

Four-point sheet resistance (SR) measurements were performed using Jandel RM3-AR setup. Native oxide was removed from all samples before measurement by dipping in 1% HF solution for 5 min followed by washing in DI water, isopropyl alcohol and drying under N_2 flow.

SiO_2 capping (by evaporation) was deposited by an electron beam evaporator (Edwards EB3) with a base pressure of ~4×10−6 Torr. SiO_2 pellets (1–5 mm, Kurt J. Lesker) were used as the evaporation source material.

SiO_2 capping by (by ALD) was deposited by an Ultratech/CNT Fiji G2 Plasma Enhanced Atomic Layer Deposition (PE-ALD). Silicon precursor was Bis(t-butylamino) silane 97% (BTBAS) and ozone as oxidizer. Process temperature was 250 °C, Argon used as a carrier gas with a base pressure of 0.2 Torr. Process sequence was as follow: 5 cycles of O_3 as a pretreatment (0.075 s pulse, 10 s Ar purge) followed by 300 cycles of 0.3 s BTBAS pulse, 8 s Ar purge, 0.15 s pulse O_3, 12 s Ar purge.

Mask preparation for R-MLD experiments was prepared using a Si wafer (280 μm thick) patterned by a standard photolithography process using AZ4562 photoresist. The patterned wafer was etched using a Bosch etch process in Oxford instruments Plasmalab 100 ICP-RIE system.

Kelvin probe force microscopy (KPFM) measurements were performed on silicon nanowires with diameter of 80 nm, contact-doped with PBA and CDB, respectively. After applying the MLCD for doping the NWs the samples were sonicated in ethanol and immediately used for drop-cast on a $Si(p^{++})/SiO_2$ (100 nm)/Si_3N_4 (100 nm) wafer. Single nanowire devices were fabricated by a single photolithography step, where a constant set of nine 2 x 2 electrodes were patterned onto the target wafer that was pre-deposited with MLCD-doped NWs. The wafers were then treated with O_2 plasma at a plasma asher to eliminate organic residues from the exposed surfaces, and with a Buffered Oxide Etch (BOE) solution to remove the native oxide formed on the Si. Then, metal contacts (10 nm Cr, 120 nm Au) were evaporated onto the surface using an electron beam evaporator. Gold was chosen as the electrode material to produce Ohmic contacts with p-type silicon.

The transfer and transconductance characteristics were measured using a Semiconductor Parameter Analyzer (SPA 4155C, *Agilent Technologies Inc.*), with the target

wafer acting as a global back-gate contact. The KPFM measurements were conducted using a Dimension Edge AFM system (*Bruker AXS*) and a Pt-Ir-coated tip, in the "dual frequency mode", where the topography is measured at the first resonance frequency (f_0) of the tip, and the contact potential difference (CPD) is measured simultaneously by electrically exciting the tip at the second resonance frequency (~ $6.2 \cdot f_0$). The CPD is the difference between the tip and sample work functions (Φ_t and Φ_s, respectively) and is defined by: $CPD = -(\Phi_t - \Phi_s)/q$, where q is the elementary charge. Throughout the KPFM measurements, the global back-gate was kept grounded. Channel lengths for electrical characterization and KPFM were ~10-25 μm.

Conflict of interest

The authors declare no competing financial interest.

Acknowledgments

This work was supported in part by the United States-Israel Binational Science Foundation grant 2012088.

References

[1] R. Yan, D. Gargas, P. Yang, *Nat. Photonics* **2009**, *3*, 569.

[2] E. D. Minot, F. Kelkensberg, M. Van Kouwen, J. A. Van Dam, L. P. Kouwenhoven, V. Zwiller, M. T. Borgström, O. Wunnicke, M. A. Verheijen, E. P. A. M. Bakkers, *Nano Lett.* **2007**, *7*, 367.

[3] W. M. Weber, A. Heinzig, J. Trommer, D. Martin, M. Grube, T. Mikolajick, *Solid. State. Electron.* **2014**, *102*, 12.

[4] X. J. Huang, Y. K. Choi, *Sensors Actuators, B Chem.* **2007**, *122*, 659.

[5] M. Law, L. E. Greene, P. Yang, *ACS Natl. Meet. B. Abstr.* **2005**, *230*, DOI 10.1146/annurev-matsci-062910-100434.

[6] A. Javey, S. W. Nam, R. S. Friedman, H. Yan, C. M. Lieber, *Nano Lett.* **2007**, *7*, 773.

[7] J. A. Czaban, D. A. Thompson, R. R. LaPierre, *Nano Lett.* **2009**, *9*, 148.

[8] X. Zhang, C. W. Pinion, J. D. Christesen, C. J. Flynn, T. A. Celano, J. F. Cahoon, *J. Phys. Chem. Lett.* **2013**, *4*, 2002.

[9] J. D. Christesen, X. Zhang, C. W. Pinion, T. A. Celano, C. J. Flynn, J. F. Cahoon, *Nano Lett.* **2012**, *12*, 6024.

[10] G. Leung, C. O. Chui, *IEEE Electron Device Lett.* **2012**, *33*, 767.

[11] D. D. D. Ma, C. S. Lee, S. T. Lee, *Appl. Phys. Lett.* **2001**, *79*, 2468.

[12] L. Pan, K. K. Lew, J. M. Redwing, E. C. Dickey, *J. Cryst. Growth* **2005**, *277*, 428.

[13] P. Das Kanungo, R. Kögler, P. Werner, U. Gösele, W. Skorupa, *Nanoscale Res. Lett.* **2010**, *5*, 243.

[14] J. C. Ho, R. Yerushalmi, Z. A. Jacobson, Z. Fan, R. L. Alley, A. Javey, *Nat. Mater.* **2008**, *7*, 62.

[15] E. C. Jones, E. Ishida, *Mater. Sci. Eng. R Reports* **1998**, *24*, 1.

[16] O. Hazut, A. Agarwala, I. Amit, T. Subramani, S. Zaidiner, Y. Rosenwaks, R. Yerushalmi, *ACS Nano* **2012**, *6*, 10311.

[17] O. Hazut, B. C. Huang, A. Pantzer, I. Amit, Y. Rosenwaks, A. Kohn, C. S. Chang, Y. P. Chiu, R. Yerushalmi, *ACS Nano* **2014**, *8*, 8357.

[18] L. Ye, A. González-Campo, R. Núñez, M. P. De Jong, T. Kudernac, W. G. Van Der Wiel, J. Huskens, *ACS Appl. Mater. Interfaces* **2015**, *7*, 27357.

[19] S. S. Chuang, T. C. Cho, P. J. Sung, K. H. Kao, H. J. H. Chen, Y. J. Lee, M. I. Current, T. Y. Tseng, *ECS J. Solid State Sci. Technol.* **2017**, *6*, P350.

[20] K. Cho, D. J. Ruebusch, M. H. Lee, J. H. Moon, A. C. Ford, R. Kapadia, K. Takei, O. Ergen, A. Javey, *Appl. Phys. Lett.* **2011**, *98*, 12.

[21] W. P. Voorthuijzen, M. D. Yilmaz, W. J. M. Naber, J. Huskens, W. G. Van Der Wiel, *Adv. Mater.* **2011**, *23*, 1346.

[22] F. Léonard, A. A. Talin, *Nat. Nanotechnol.* **2011**, *6*, 773.

[23] S. R. McKibbin, G. Scappucci, W. Pok, M. Y. Simmons, *Nanotechnology* **2013**, *24*, DOI 10.1088/0957-4484/24/4/045303.

[24] C. Garozzo, F. Giannazzo, M. Italia, A. La Magna, V. Privitera, R. A. Puglisi, *Mater. Sci. Eng. B Solid-State Mater. Adv. Technol.* **2013**, *178*, 686.

[25] E. Y. J. Kong, P. Guo, X. Gong, B. Liu, Y. C. Yeo, *IEEE Trans. Electron Devices* **2014**, *61*, 1039.

[26] J. Veerbeek, L. Ye, W. Vijselaar, T. Kudernac, W. G. Van Der Wiel, J. Huskens, *Nanoscale* **2017**, *9*, 2836.

[27] J. O'Connell, G. A. Verni, A. Gangnaik, M. Shayesteh, B. Long, Y. M. Georgiev, N. Petkov, G. P. McGlacken, M. A. Morris, R. Duffy, J. D. Holmes, *ACS Appl. Mater. Interfaces* **2015**, *7*, 15514.

[28] L. Ye, S. P. Pujari, H. Zuilhof, T. Kudernac, M. P. De Jong, W. G. Van Der Wiel, J. Huskens, *ACS Appl. Mater. Interfaces* **2015**, *7*, 3231.

[29] S. R. McKibbin, C. M. Polley, G. Scappucci, J. G. Keizer, M. Y. Simmons, *Appl. Phys. Lett.* **2014**, *104*, DOI 10.1063/1.4869111.

[30] R. C. Longo, K. Cho, W. G. Schmidt, Y. J. Chabal, P. Thissen, *Adv. Funct. Mater.* **2013**, *23*, 3471.

[31] J. H. Yum, H. S. Shin, R. Hill, J. Oh, H. D. Lee, R. M. Mushinski, T. W. Hudnall, C. W. Bielawski, S. K. Banerjee, W. Y. Loh, W. E. Wang, P. Kirsch, *Appl. Phys. Lett.* **2012**, *101*, 1.

[32] L. Mathey, T. Alphazan, M. Valla, L. Veyre, H. Fontaine, V. Enyedi, K. Yckache, M. Danielou, S. Kerdiles, J. Guerrero, J. P. Barnes, M. Veillerot, N. Chevalier, D. Mariolle, F. Bertin, C. Durand, M. Berthe, J. Dendooven, F. Martin, C. Thieuleux, B. Grandidier, C. Copéret, *J. Phys. Chem. C* **2015**, *119*, 13750.

[33] Z. Sun, O. Hazut, B. C. Huang, Y. P. Chiu, C. S. Chang, R. Yerushalmi, L. J. Lauhon, D. N. Seidman, *Nano Lett.* **2016**, *16*, 4490.

[34] O. Hazut, R. Yerushalmi, *Langmuir* **2017**, *33*, 5371.

[35] S. Yitzchaik, R. Gutierrez, G. Cuniberti, R. Yerushalmi, *Langmuir* **2018**, *34*, 14103.

[36] A. Agarwala, T. Subramani, A. Goldbourt, D. Danovich, R. Yerushalmi, *Angew. Chemie - Int. Ed.* **2013**, *52*, 7415.

[37] J. A. Faniran, H. F. Shurvell, *Can. J. Chem.* **1968**, *46*, 2089.

[38] P. J. Linstrom, W. G. Mallard, *NIST Chemistry Webbook*, **2015**.

[39] H. G. Francois-Saint-Cyr, F. A. Stevie, J. M. McKinley, K. Elshot, L. Chow, K. A. Richardson, *J. Appl. Phys.* **2003**, *94*, 7433.

[40] E. R. Lory, R. F. Porter, *J. Am. Chem. Soc.* **1971**, *93*, 6301.

[41] R. Nishiyabu, Y. Kubo, T. D. James, J. S. Fossey, *Chem. Commun.* **2011**, *47*, 1124.

[42] O. Hazut, A. Agarwala, T. Subramani, S. Waichman, R. Yerushalmi, *J. Vis. Exp.* **2013**, *82*, e50770.

TOC

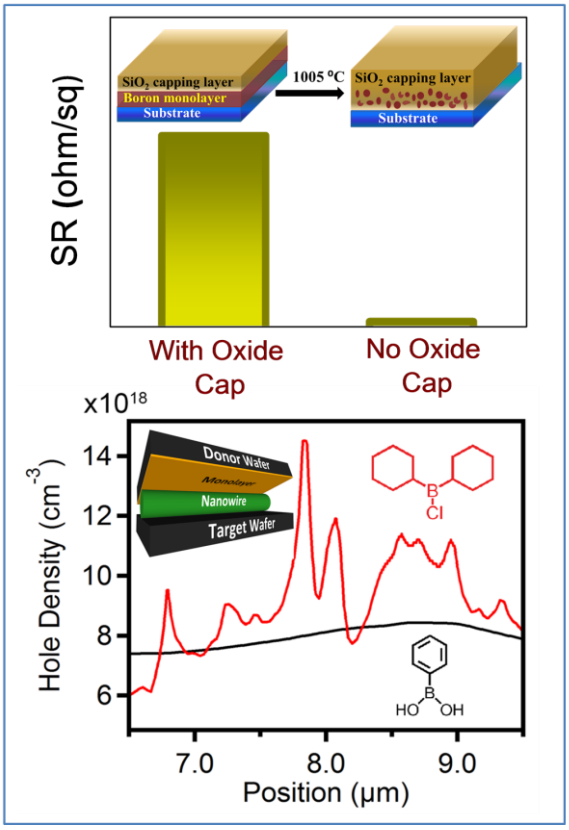
SR (ohm/sq)
SiO2 capping layer
Boron monolayer
Substrate
1005 °C
SiO2 capping layer
Substrate
With Oxide Cap
No Oxide Cap
x10^18
Hole Density (cm^-3)
14
12
10
8
6
Donor Wafer
Monolayer
Nanowire
Target Wafer
B
Cl
HO
OH
7.0
8.0
9.0
Position (μm)